Contents lists available at ScienceDirect

Applied Catalysis B: Environmental

journal homepage: www.elsevier.com/locate/apcatb

Achieving long-lived shallow trapping states in carbon nitride through the n-π*electronic transition for enhanced photocatalytic hydrogen generation

Yan Chen [a], Yingpeng Cheng [b], Yue Liu [a], Yaqian Wang [a], Yi Qu [a], Daochuan Jiang [b,*], Zhaozhao Qin [c,*], Yupeng Yuan [b,*]

[a] School of Chemistry and Chemical Engineering, and the Key Laboratory of Structure and Functional Regulation of Hybrid Materials (Anhui University), Ministry of Education, Anhui University, Hefei 230601, PR China
[b] School of Materials Science and Engineering, Anhui University, Hefei 230601, PR China
[c] Henan Key Laboratory of Infrared Materials & Spectrum Measures and Applications, School of Physics, Henan Normal University, Xinxiang 453007, PR China

ARTICLE INFO

ABSTRACT

The presence of short-lived shallow trapping states in semiconductor-based photocatalysts hinders efficient utilization of charge carrier, which compromises the solar-to-hydrogen efficiency. Here, we presented an engineered graphitic carbon nitride (g-CN) nanosheets with long-lived shallow trapping states achieved through an n-π * electronic transition. This transition induces a significant red-shifted absorption edge at 600 nm, effectively extending the range of light absorption compared to pristine g-CN. Moreover, the engineered g-CN nanosheets exhibit lower exciton binding energies (36 meV) compared to pristine counterparts (50.1 meV), as revealed by temperature-dependent photoluminescence (PL) spectra. Femtosecond transient absorption spectroscopy (fs-TAS) confirms the presence of long-lived shallow trapping states (lifetime: 565.8 ps) in the engineered g-CN nanosheets. These states enable a greater participation of photoinduced electrons in photocatalytic reactions, resulting in significantly enhanced photoactivity. Notably, the g-CN sample with the n-π * transition achieves a remarkable photocatalytic H_2 production rate of 61.8 μmol h^{-1}, which is a fivefold enhancement over pristine g-CN nanosheets. These findings highlight the crucial role of the n-π * transition in g-CN for prolonging shallow electron trapping and ultimately leading to superior photocatalytic performance.

1. Introduction

Photocatalytic H_2 production using semiconductor-based photocatalysts represents a promising approach to harness abundant solar energy for green hydrogen fuel generation, addressing environmental pollution and energy shortages [1–6]. Over the last few decades, extensive research has been devoted to developing efficient photocatalysts for H_2 production under UV–visible light irradiation, with materials like TiO_2 [7], CdS [8], and their derivatives [9,10] being explored. g-CN has emerged as an attractive candidate due to its well-matched energy band for water splitting, resilience to thermal and chemical infulences, and ease of functionalization [11,12]. Nevertheless, pristine g-CN faces challenges related to high charge recombination rates, primarily stemming from the short lifetime of excited states, particularly shallow trapping states [13]. Investigations into the kinetics of photoexcited charge carriers within g-CN have identified three trapping mechanisms: nascent excitons, shallow trapping states, and deep

trapping states [14,15]. While nascent excitons are prone to annihilation, deep trapping states do not faciliate splitting water. Therefore, shallow trapping states play a crucial role in enhancing the photocatalytic activity. Extending the lifetime of shallow trapping in g-CN is a key approach for enhancing its photocatalytic performance [16]. However, this aspect has received relatively limited attention in previous research.

To address the challenge of short-lived shallow trapping states in g-CN, various strategies have been explored, such as forming heterojunctions with other photocatalysts [17], exfoliating bulk g-CN into nanosheets [18], functionalizing with metal nanoparticles like Pt [19], and engineering the band structure of g-CN by incorporating heteroatoms including B, S, N, and P [20–23]. Our recent work demonstrated that utilizing the n-π * electronic transition in g-CN showed promise for suppressing charge recombination while simultaneously expanding the light absorption range [24]. Theoretical calculations have identified two electronic transitions within g-CN: π-π * and n-π *, corresponding to the

excitation of electrons from the bonding orbitals (π) and lone pairs of edge N atoms in tri-s-triazine units to to antibonding orbitals (π *), respectively. Notably, the enegy level of lone-pair (n) electrons in g-CN is higher than that of the bonding orbitals (π), making it energetically more favorable for the n-π * transition compared to the π-π * transition. As a result, these transitions produce the absorption edges at around 460 nm and 600 nm, respectively [25]. The n-π * transition is specifically viable in corrugated or asymmetrical tri-s-triazine units. It influences the electronic structure of g-CN, potentially reducing charge recombination by increasing the repulsion among lone-pair electrons due to their reduced inter-distance [26]. To date, various methods have been explored to facilitate this transition, including microwave-assisted heating [24], disrupting hydrogen bonding between melon strands in g-CN [27], stepwise pyrolysis of urea at elevated temperatures [28], and copolymerization with other precursors (e.g., triazole) [29]. However, despite these efforts, there are currently no studies reporting the impact of the n-π * transition on the trapping states within photoexcited g-CN.

In this study, we investigated the decay dynamics of g-CN with a pronounced n-π * transition using femtosecond transient absorption spectroscopy. The g-CN with an n-π * transition was synthesized by heating the urea-NTC aggregates in a furnace at 550 °C for 3 h. Using urea-NTC aggregates as a starting precursor not only produced g-CN nanosheets [30], but also effectively incorporated sulfur (S) into the tri-s-triazine units. The S atom replaces the N at the edge of the tri-s-triazine units, disrupting their planar symmetry and inducing the n-π * transition. The fs-TAS measurements revealed a remarkble extension of the shallow electron trapping lifetime ($\tau = 565.8$ ps) in the n-π * transition engineered g-CN, exceeding pristine g-CN ($\tau = 129.6$ ps). As a result of the n-π * transition, the resulting g-CN nanosheets exhibited a considerable red-shifted absorption edge, extending it from the original 460 nm of pristine g-CN to approximately 600 nm. Importantly, these g-CN nanosheets engineered with n-π * transition demonstrated a remakable H_2 production rate of 61.8 μmol h^{-1}, approximately 5.2 times higher than the H_2 production rate of pristine g-CN without the n-π * transition (11.8 μmol h^{-1}).

2. Experimental section

2.1. Chemicals and materials

The following chemicals were used: urea, 5-Nitro-2-thiophenecarboxaldehyde (NTC), terephthalic acid (TPA), NaOH, and triethanolamine (TEOA), all of which were obtained from Aladdin Industrial Inc. Chloroplatinic acid was acquired from Sinopharm Reagent Network. Unless otherwise noted, all chemicals were directly used as received without additional purification.

2.2. Synthesis of S-doped g-CN nanosheets

A crucible containing 20 g of urea was placed in an oil bath and heated to 150 °C until the urea melted into a liquid state. Subsequently, different amounts of NTC (10, 20, and 30 mg) were added to the urea liquid and vigorously mixed to form a homogeneous brown solution (labeled as UNTC$_m$, where m=10, 20, and 30, representing the mass of NTC used) (see Fig. S1). After cooling to room temperature, the resulting solid was directly subjected to calcination in a muffle furnace at 550 °C for 3 h, with a temperature ramp of 5 °C min^{-1}. The yielded materials were labeled as g-CN/S-x (x = 10, 20, and 30, corresponding to the mass of NTC added). For comparison, the reference g-CN was also prepared using the same condition, but without the addtion of NTC, and the resulting product was denoted as g-CN.

3. Results and discussion

The synthesis of g-CN nanosheets engineered with the n-π * transition involves the preorganization of the urea-NTC aggregates in an oil

bath, followed by thermolysis in a muffle furnace, as depicted in Fig. 1a. Initially, urea was heated in an oil bath at 150 °C, resulting in the formation of a liquid state. Different amounts of NTC were then added, leading to the production of brown aggregates (Fig. S1). First, the formation of aggregates was visualized by the distinct morphological changes of the urea. Pristine urea had an irregular bulk structure (Fig. S2a), but upon treatment in an oil bath, sheet-like structures were formed (Fig. S2b). Addition of NTC (Fig. S2c) significantly promoted the self-assembly of urea, transforming it from sheet-like to belt-like structures (Fig. 1b). This observation confirms the effective interaction between urea and NTC, as their structure integrity was preserved after melting in the oil bath (see Fig. S3).

The aggregates, denoted as UNTC$_m$ (m=10, 20, and 30, corresponding to the mass of NTC added), are mainly composed of urea, as verified by the FT-IR spectra (Fig. S4a), which shows no remarkable difference between UNTC$_{20}$ and pure urea. However, subtle differences were observed, such as a weak stretching vibration peak of aromatic –NO$_2$ at 1330 cm^{-1}, indicating the presence of NTC in UNTC$_{20}$ [31]. This presence of NTC was further confirmed by XPS analysis (Fig. S4b-S4f), where the elements of C, N, O, and S were observed in the XPS survey spectrum of UNTC$_{20}$ (Fig. S4b). The distinctive peak of S 2p at approximately 164 eV provides clear evidence of the thiophene group, with peaks corresponding to C–S–C, S–C–N, and S–O bonds (Fig. S4f) [32].

Subsequently, the UNTC$_m$ aggregates were thermally treated in a muffle furnace at 550 °C for 3 h to obtain the S-doped g-CN nanosheets (g-CN/S-x). A reference sample of g-CN was also prepared by direct heating of urea obtained after melting under the same conditions. The SEM and TEM images of neat g-CN and g-CN/S-20 are presented in Fig. 1and Fig. S5. The g-CN sample exhibits sheet-like structures and their stacked arrangements (Fig. S5a). In stark contrast, g-CN/S-20 displays ultrathin nanosheet structures (Fig. 1c), suggesting the effective alteration of g-CN morphology by NTC addition (Fig. S6a, b). In TEM images, g-CN appears nontransparent (Fig. S5b), whereas g-CN/S-20 shows almost transparent feature with curled and ragged edges (Fig. 1d), confirming the ultrathin nanosheet structure. The observed curvature in the nanosheets (arrows in Fig. 1d) reflects the corrugation of tri-s-triazine units in g-CN/S-20. TEM elemental mapping (Fig. 1e) confirms the homogeneous distribution of doped S in the g-CN/S-20 sample. The thickness of the nanosheets was approximately 2.42 nm (Figs. 1f, 1g), equivalent to 7 at. layers [33]. In contrast, g-CN has a thickness of $\sim$ 4.80 nm (Fig. S7a and b).

These nanosheets provide the g-CN/S-x samples with an increased surface area in contrast to g-CN. Particularly, the g-CN/S-20 sample shows a broad range of pore sizes spanning from 2 to 70 nm (the inset of Fig. 1h). The surface area of the g-CN/S-20 sample is approximately 90.7 m^2 g^{-1}, nearly 1.5 times larger than that of g-CN (61.0 m^2 g^{-1}) (Table S1). These results confirm the ultrathin and porous nanosheets structure of the g-CN/S-20 sample. Moreover, g-CN/S-20 sample exhibits a slightly higher decomposition temperature than g-CN (Fig. 1i), suggesting that S-incorporation improves the thermal stability of g-CN.

The crystal structure and chemical states of the g-CN and g-CN/S-20 samples were analyzed using XRD, FT-IR, XPS, Raman, and NMR spectroscopy. XRD patterns of the four samples (Fig. S8a) display similar peak patterns, indicating the essentially same frameworks. The XRD peaks observed at 13.1° and 27.3° correspond to the ordered stacking of both in-plane and interlayer structure, respectively [34]. Notably, the intensity of the (1 0 0) peak gradually decreases with increasing amounts of NTC. This observation is likely the impairing of the hydrogen bonds in g-CN/S-20 samples due to the smaller electronegativity of S compared to N. Furthermore, a visible decrease in the intensity of the (0 0 2) peak is observed, reflecting the reduced crystallinity of g-CN due to the breakage of hydrogen bonds (Fig. S8a) [35]. The (0 0 2) peak slightly shifts from 27.6° in g-CN to 27.2° in g-CN/S-20 (Fig. 2a), suggesting an increase in the interlayer distance due to the larger size of S atoms compared to N atoms [36,37]. Based on previous reports[18,35], we
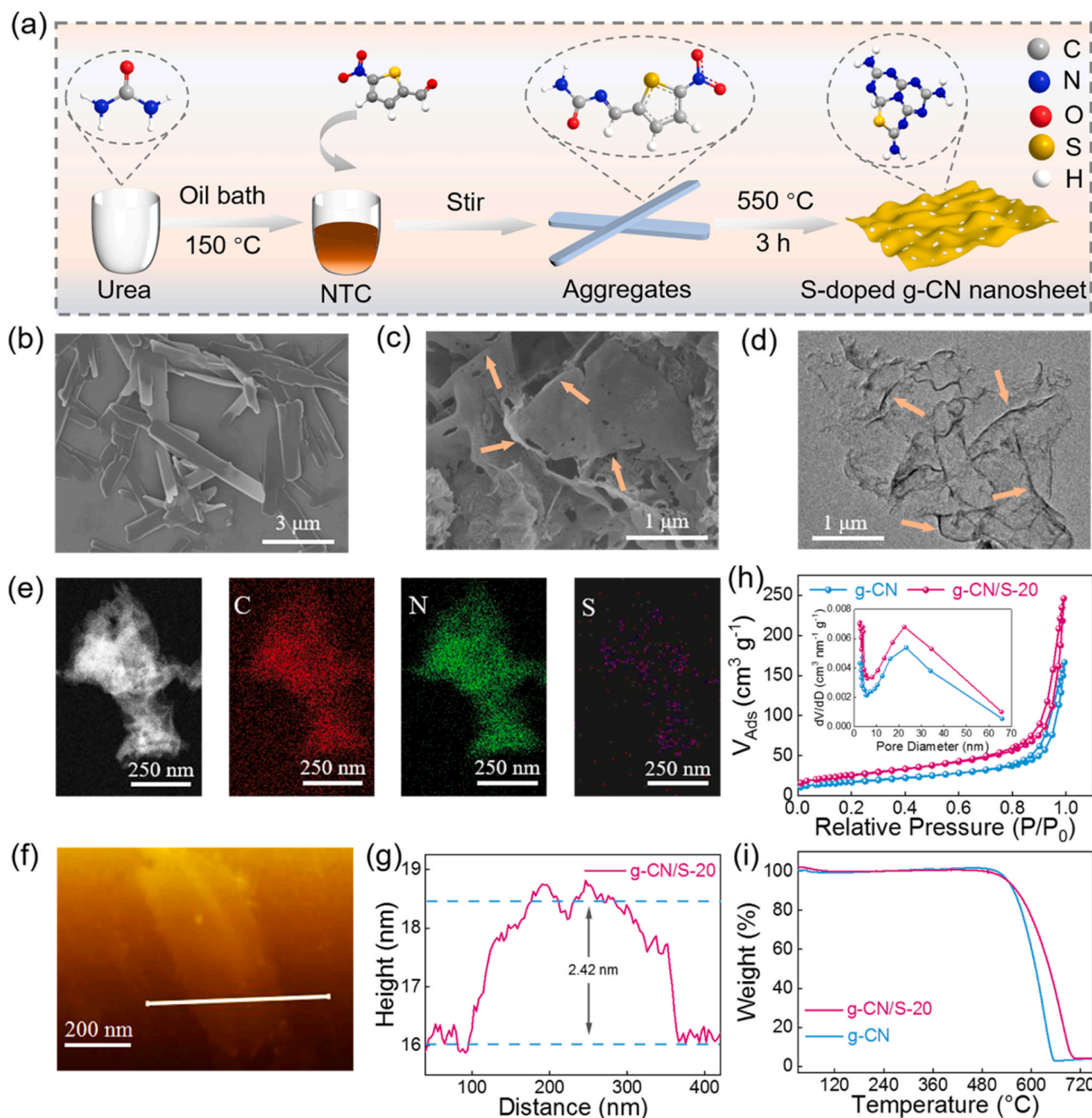
Fig. 1. (a) Process for preparing g-CN/S-x nanosheets. SEM images of (b) UNTC$_{20}$ aggregates, and (c) g-CN/S-20. (d) TEM images of g-CN/S-20. (e) TEM bright-field image and elemental mapping (C, N, and S) of g-CN/S-20. (f) AFM image of g-CN/S-20 nanosheets. (g) Thickness analysis. (h) N$_2$ adsorption-desorption isotherms with pore size distribution curves (inset). (i) TG curves of g-CN and g-CN/S-20.

selected the edge of N as the substitution site for S dopant in this study, a choice supported by the ^{13}C NMR spectrum and the S 2p XPS spectrum. The FT-IR spectra of different samples (Fig. S8b) show typical vibration bands between 1200 cm^{-1} and 1650 cm^{-1}, ascribed to the C–N heterocycles. A sharp peak at 813 cm^{-1} indicates the stretching vibrations of the tri-s-triazine units. The N–H stretching vibrations (e.g. –NH$_2$ or –NH groups) are visible within the range of 3000 cm^{-1} to 3400 cm^{-1} [38]. Notably, a closer examination of the absorption band between 1150 cm^{-1} and 1600 cm^{-1} reveals three relatively weakened absorption peaks at 1276, 1335, and 1431 cm^{-1} in g-CN/S-20 (Fig. 2b). These alterations in the FT-IR spectrum are attributed to the structural distortion caused by the incorporation of S, resulting in the asymmetry of the tri-s-triazine units, as reported in the literature [24,39]. For g-CN and g-CN/S-20, the peaks at 985 and 705 cm^{-1} in Raman spectra (Fig. S9)

were attributed to the symmetric N-breathing mode and the in-plane bending of tri-s-triazine units. In addition, the characteristic peaks at 1150–1750 cm^{-1} are associated with the disordered graphitic C–N vibrations [40].

The chemical structure of the g-CN and g-CN/S-20 samples was further examined using NMR spectra. Two resonance peaks at δ_1 = 164.95 and δ_2 = 156.57 ppm (Fig. 2c) observed in both g-CN and g-CN/S-20 are attributed to the C1 and C2 atoms in tri-s-triazine units (Fig. S10), respectively [41]. Notably, the g-CN/S-20 sample exhibits an additional peak at 163.37 ppm compared to the g-CN sample (Fig. S10). This peak is attributed to the C3 atoms that are linked to –NH– groups in g-CN [42]. This observation reveals that the chemical environment of C was affected by the incorporated S in g-CN/S-20. The ^{15}N NMR spectrum of g-CN/S-20 presents distinct resonances (Fig. 2d). Two strongest peaks
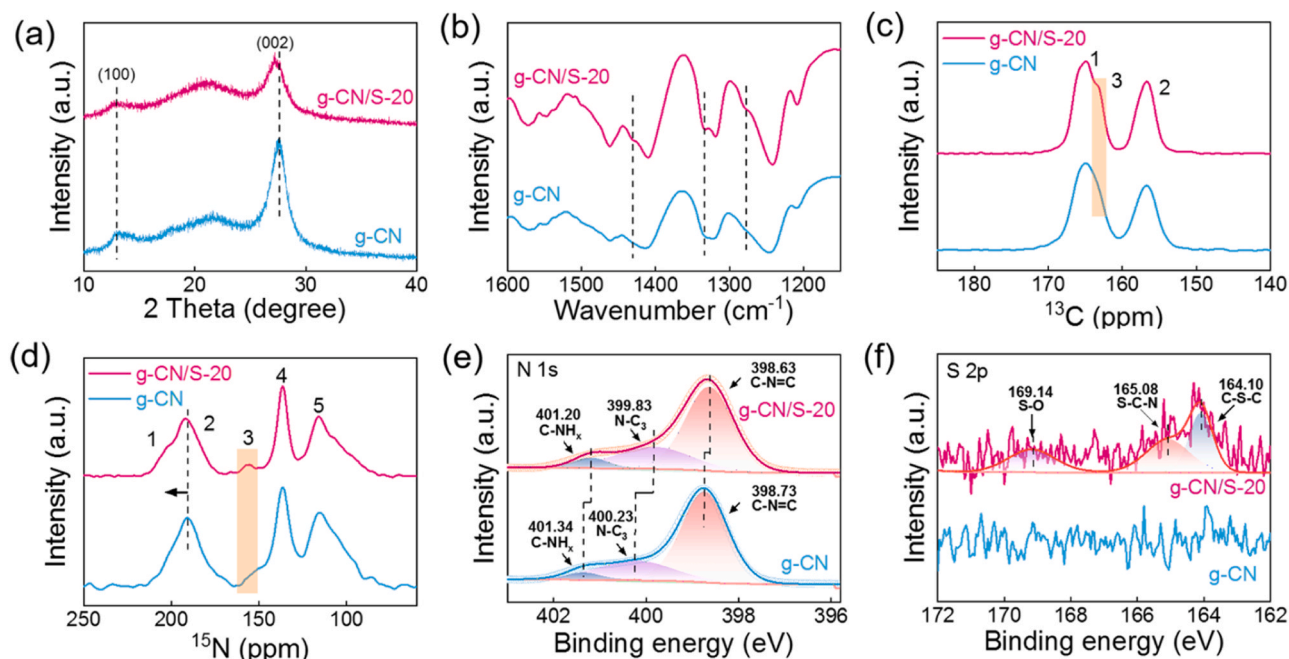
Fig. 2. (a) XRD patterns, and (b) FT-IR spectra (1150–1600 cm^{-1}) of g-CN and g-CN/S-20. Solid-state MAS NMR spectra: (c) ^{13}C, (d) ^{15}N of the g-CN and g-CN/S-20. (e) N 1 s, and (f) S 2p XPS spectra for g-CN and g-CN/S-20.

at $\delta_4 = 136.33$ ppm (N4) and $\delta_5 = 115.59$ ppm (N5) originate from the N atoms in the –NH– and –NH$_2$ groups, respectively [43]. Additionally, two asymmetric peaks at $\delta_1 = 203.00$ ppm (N1) and $\delta_2 = 190.56$ ppm (N2) are ascribed to the N atoms in proximity to the –NH– and –NH$_2$ groups within the C–N = C structure, respectively. Noticeably, the N2 peak in g-CN/S-20 is slightly shifted when compared to g-CN, likely due to the S-incorporation within the g-CN framework. The weakest peak at $\delta_3 = 156.11$ ppm (N3) corresponds to the N atoms situated at the center of the tri-s-triazine units [44]. Significantly, the intensity of the N3 peak is notably heightened in g-CN/S-20 compared to that of g-CN. This enhancement results from the distortion of the tri-s-triazine units, which effectively shortens the spacing between N3 and the adjacent –NH–/–NH$_2$ groups [45]. In conclusion, the above analysis collectively validates on the subtle structural changes of tri-s-triazine units in g-CN/S-20, rendering the n-π * electronic transition feasible.

XPS measurements were used to further analyze the surface chemical states of the g-CN and g-CN/S-20 samples. The XPS survey spectra of g-CN and g-CN/S-20 are almost discernable due to the low amounts of S in g-CN/S-20 (Fig. S11a). Deconvolution of the C 1 s binding energy (Fig. S11b) unveils three peaks at 284.80, 286.2, and 288.11 eV, representing graphitic carbon (C=C/C–C), C–S, and sp^2 hybridized C (N–C=N), respectively [46]. The N 1 s spectrum of g-CN (Fig. 2e) exhibits deconvoluted peaks at 398.73, 400.23, and 401.34 eV, assigning to C=N–C, N–C$_3$, and C–NH$_X$, respectively. Notably, the corresponding peaks in the g-CN/S-20 sample show an obvious negative shift, representing a result of the S incorporation into the framework of g-CN/S-20 [47,48]. The S 2p spectrum of g-CN/S-20 (Fig. 2f) exhibits a peak at 164.10 eV, which is attributed to the C–S–C bonds in tri-s-triazine units [32,49]. The peak at 165.08 eV is ascribed to S–C–N bonds [32], while the peak at 169.14 eV is the S–O bonds, likely originating from the surface-adsorbed oxygen or other oxygen-containing functional groups [40]. For g-CN, the C/N molar ratio is 0.67, less than 0.72 for g-CN/S-20 sample (Table S2). This result is consistent with elemental analysis (EA) results (Table S3). It can be noticed the C/N molar ratios of samples increase from 0.67 to 0.91 with an increase in NTC amounts, which is accompanied by a gradual increase in the S content from 0 to 0.30. Specifically, the XRD, FT-IR NMR, and XPS spectra clearly confirm that S substitutes for the N at the edge of tri-s-triazine, causing structural

asymmetry of the tri-s-triazine units, which allow the n-π * transition.

The structure changes in g-CN directly influence its light absorption properties. As shown in Fig. 3a, S-incorporation leads to the emergence of an additional peak at around 480 nm in the UV–vis spectra. In contrast to the absorption edge of pristine g-CN at ~ 460 nm, the g-CN/S-20 sample exhibits a markedly extended light absorption within the visible light spectrum, with an emerging absorption peak at ~ 480 nm. This peak is indicative of the n-π * electronic transition in g-CN [25], which expands the absorption edge of g-CN/S-20 to approximately 600 nm. Moreover, the peak intensity of the n-π * electronic transition becomes more pronounced with increased S amounts (Fig. S12a). The color of g-CN/S-x samples gradually darkens with the increase in S content, consistent with this enhanced light absorption behavior (see inset in Fig. S12a).

The n-π * electronic transition regulates the electronic structure of g-CN, thereby influencing its photoelectrochemical performance, as demonstrated by the Mott-Schottky measurements (Fig. S12b). The positive slope in the Mott-Schottky plots represent a n-type semiconductor of both g-CN and g-CN/S-20 samples [50]. The flat band potentials were measured to be − 1.35 and − 1.25 V (vs. Ag/AgCl) for g-CN and g-CN/S-20, respectively. Given that the conduction band bottom (E$_{cb}$) is approximately 0.3 eV below that of the flat potential [51], the determined E$_{cb}$ for g-CN and g-CN/S-20 samples is − 1.45 and − 1.35 V (vs. NHE), respectively. By comparing Tauc plots (Fig. S12c), the energy positions of E$_{cb}$ and E$_{vb}$ (valence band) of g-CN and g-CN/S-20 are then drawn in the inset of Fig. S12b. It is evident that the photoexcited electrons in g-CN and g-CN/S-20 are thermodynamically favorable for reducing H$^+$ to generate H$_2$.

To demonstrate the impact of n-π * transition on the photocatalytic activity, we subsequently conducted tests to evaluate the photocatalytic H$_2$ generation under visible light illumination (Fig. 3b, Fig. S13a). The g-CN sample shows a moderate H$_2$ rate of 11.8 μmol h^{-1} (Fig. 3b). The incorporation of S significantly increases the H$_2$ generation activity. For instance, the g-CN/S-10 sample, with a low S content, displays a remarkable H$_2$ production rate of 43.2 μmol h^{-1}. Furthermore, g-CN/S-20 with an optimum S amount exhibits the highest H$_2$ rate of 61.8 μmol h^{-1}, up to 5.2-fold enhancement compared to the g-CN sample (see the inset in Fig. 3b). This enhanced H$_2$ generation is
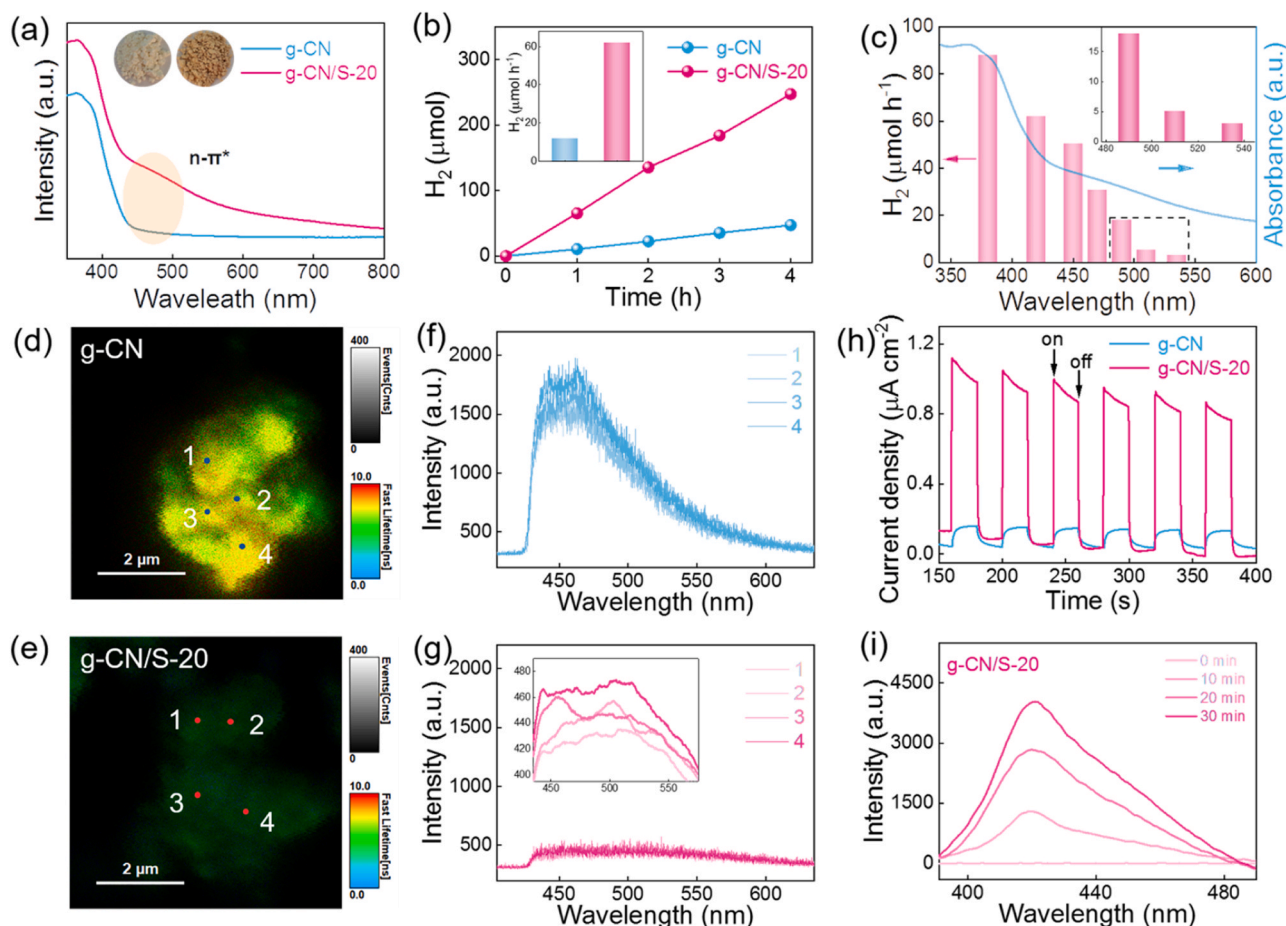
Fig. 3. (a) UV–visible absorption spectra of g-CN and g-CN/S-20. (b) Photocatalytic H_2 generation of g-CN and g-CN/S-20, with the inset illustrating the average H_2 production rate within four hours. (c) Wavelength-dependent H_2 production by g-CN/S-20. Single-particle PL images of (d) g-CN, (e) g-CN/S-20, and their PL spectra of (f) g-CN, and (g) g-CN/S-20. The inset in (g) shows an enlarged view of the PL spectra of g-CN/S-20. (h) Transient photocurrent response of g-CN and g-CN/S-20. (i) Fluorescence spectra of a TAOH solution generated by 0.05 g of g-CN/S-20 after different irradiation time.

primarily ascribed to the n-π * electronic transition. However, excessive S-incorporation leads to a reduced H_2 generation as the incorporated S reversely acts as the recombination centers for photoexcited charge carriers and impedes their transport [35]. Control experiments were performed without TEOA as the hole scavenger or Pt as the cocatalyst. Only a small amount of H_2 was detected in both cases, indicating the crucial role of TEOA and Pt (Fig. S13b). Fig. S13c displays the effect of Pt amounts on g-CN/S-20 for photocatalytic H_2 production under visible light irradiation, which shows that the highest photocatalytic H_2 production rate of 72.3 μmol h^{-1} was obtained over 2 wt% Pt loaded g-CN/S-20. Considering this little difference in the photocatalytic performance between 0.5 wt% Pt and 2 wt% Pt loaded g-CN/S-20, the selection of 0.5 wt% Pt as cocatalysts was considered economically in this work. Meanwhile, to illustrate the effect of oil-bath treatment on the photocatalytic H_2 production of g-CN, g-CN was synthesized by a physical mixture of urea (20 g) and NTC (20 mg) at 550 °C for 3 h (named g-CN/S-20-PM) and its photocatalytic H_2 production was measured under the same conditions. Remarkably, the H_2 production rate of g-CN/S-20 is about 2 times higher than that of g-CN/S-20-PM. (33.1 μmol h^{-1}) (Fig. S13d). It is worth noting that the photocatalytic performance demonstrated in this work is superior to many reported g-CN-based photocatalysts in the literature (Fig. S14).

Wavelength-dependent H_2 generation was conducted to examine the impact of the n-π * electronic transition on photocatalytic performance (Fig. 3c). As expectd, the n-π * transition has a positive effect on photocatalytic H_2 production. For instance, the g-CN/S-20 sample can actively produce H_2 (30.8 μmol h^{-1}) when exposed to light with a

wavelength above 470 nm. In stark contrast, pristine g-CN did not produce H_2 when irradiated with light above 470 nm because this cutoff wavelength exceeds its absorption edge (~ 460 nm). The longest cutoff wavelength for H_2 generation is observed to be 535 nm for the g-CN/S-20 sample (see the inset in Fig. 3c). Hence, the wavelength-dependent H_2 generation demonstrates the beneficial effect of the n-π * transition in enhancing photocatalytic performance.

The stability of the g-CN/S-20 sample was also examined through cycling reactions, as shown in Fig. S15a. It is worth noting that g-CN/S-20 sample exhibits a slightly decreased H_2 production after four consecutive runs (total 12 h) (Fig. S15a). This decrease in H_2 production is likely due to the operation issues, possibly indlucing higher gas pressure within the reactor resulting from Ar degassing before each cycle. Notably, the extended H_2 generation using the g-CN/S-20 sample demonstrates a proportional relationship between H_2 production and irradiation time, suggesting excellent photocatalyst durability (Fig. S15b). After long-term photocatalytic H_2 generation, the XRD pattern, FT-IR spectra, and SEM of the g-CN/S-20 sample remain unchanged compared to those before the photocatalytic reactions (Fig. S16). This observation provides further evidence for the preservation of the g-CN framework.

To assess the impact of the n-π * transition on charge transfer in g-CN, we conducted single-particle photoluminescence (PL) measurements, as illustrated in Fig. 3d–g. During the measurements, a 405 nm laser was used for excitation. The PL spectra in Fig. 3f and g were obtained from the marked positions in Fig. 3d and e, respectively. The g-CN sample exhibits a prominent PL intensity at around 450 nm. In contrast,

this PL peak is significantly reduced in the g-CN/S-20 sample, signifying a notable suppression of electron–hole pair recombination [52]. Notably, the red-shifted PL peak from 450 nm in g-CN to 490 nm in g-CN/S-20 (as depicted in the inset of Fig. 3g) supports the influence of the n-π * electronic transition on charge transfer and recombination in g-CN, as previously elucidated [53]. Additionally, the average lifetimes of charge carriers were measured to be 2.23 and 0.69 ns for g-CN and g-CN/S-20, respectively (Fig. S17). The shorter lifetime indicates faster transfer of photoexcited charge carriers in g-CN/S-20 compared to g-CN, which is consistent with the PL result. The higher charge carrier separation efficiency in g-CN/S-20 was further supported by the transient photocurrent measurements (Fig. 3h) [54]. The g-CN/S-20 sample shows a fast photocurrent response and remarkably higher photocurrent density compared to the g-CN sample, suggesting a significantly enhanced separation of electrons and holes. This is further supported by electrochemical impedance spectroscopy (EIS) and linear scanning voltammetry (LSV) measurements. The g-CN/S-20 sample exhibits a smaller arc radius in the Nyquist plots (Fig. S18a), indicating lower resistance for charge transfer compared to g-CN. The LSV curves display a positive shift in the g-CN/S-20 sample, suggesting a lower over-potential for hydrogen evolution reaction (HER) (Fig. S18b). The n-π * transition also induces a more intense EPR signal (particularly under light irradiation) for g-CN/S-20 compared to g-CN (Fig. S18c), indicating the presence of more unpaired electrons in the g-CN/S-20 sample [3].

To further confirm the enhanced electron and hole separation in g-CN/S-20, we employed a terephthalic acid (TPA)-based PL method to detect photogenerated •OH. The reaction between TPA molecules and •OH can produce 2-hydroxyterephtalic acid (TAOH), which emits a PL peak at 430 nm. As illustrated in Fig. 3i and S19, the intensity of this PL peak increases with prolonged irradiation time for both the g-CN and g-CN/S-20 samples, indicating an increase in •OH concentration with extended light exposure. Importantly, at the same irradiation time, the g-CN/S-20 system displays a significantly higher PL peak intensity than the g-CN system (Fig. 3i). In summary, the g-CN/S-20 photocatalyst has a stronger ability to produce •OH compared to the g-CN sample [55].

The incorporation of S heteroatoms significantly increases light absorption above λ ≥ 460 nm, leading to an elevated temperature in the H₂ generation reactor, thereby improving the photocatalytic reaction. Infrared camera measurements of surface temperature after 1 h of light irradiation showed that the reactor containing g-CN reaches approximately 40 °C, while the g-CN/S-20 system reaches 47 °C. This result demonstrates the advantageous effect of S-incorporation in raising the temperature for photocatalytic reactions (Fig. S20a) [56]. The rising temperature was more evident in the infrared photos (Fig. S20b).

To investigate the exciton properties in g-CN/S-20, we performed temperature-dependent PL measurements. As the temperature increased from 77 to 253 K, both g-CN and g-CN/S-20 exhibited decreased PL intensity due to thermally activated nonradiative recombination process (Fig. 4a, b) [57]. We then calculated the exciton binding energy using the following equation:
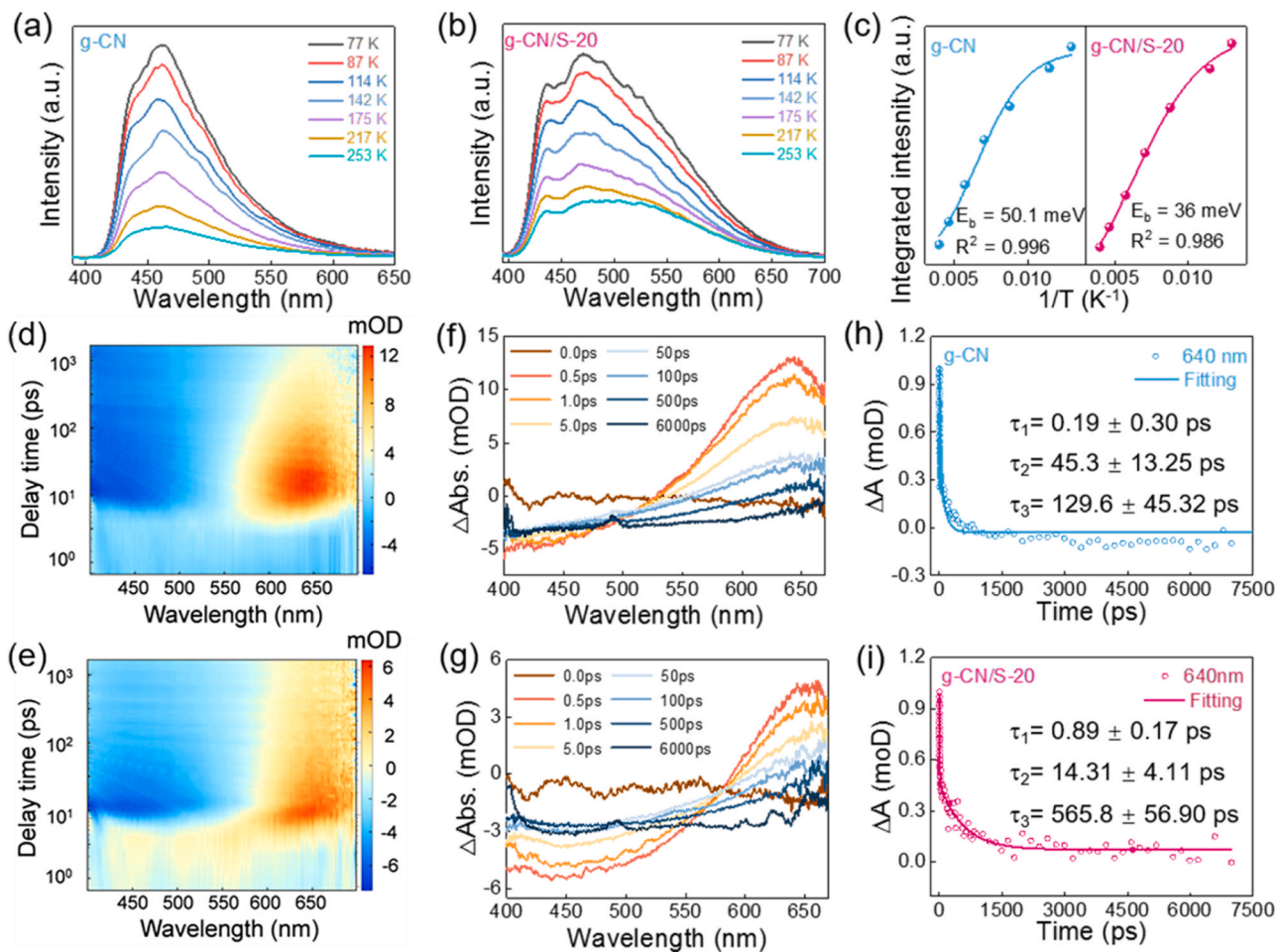
$$I(T) = \frac{I_0}{1 + Ae^{-E_b/k_BT}}$$

Fig. 4. Temperature-dependent PL spectra for (a) g-CN, and (b) g-CN/S-20. (c) The extracted exciton binding energies of g-CN (left panel) and g-CN/S-20 (righ panel). 2D pseudo-color maps of (d) g-CN, (e) g-CN/S-20, and their corresponding fs-TA spectra under several representative probe delays: (f) g-CN, and (g) g-CN/S-20. Kinetics decay profile probed at 640 nm of (h) g-CN, and (i) g-CN/S-20.

where I_0 is the intensity at 0 K, A is a proportional constant, E_b is the binding energy, and k_B is the Boltzmann constant [58]. Fitting these experimental data revealed exciton binding energies of 50.1 meV for g-CN and 36.0 meV for g-CN/S-20 (Fig. 4c). This result indicates that the excitons in g-CN/S-20 are more prone to dissociation compared to g-CN, resulting in a higher number of free charge carriers in g-CN/S-20 and contributing to its enhanced photocatalytic activity [59].

We also conducted femtosecond transient absorption spectroscopy (fs-TAS) to investigate the influence of the n-π * transition on the decay dynamics of excited charge carriers in g-CN and g-CN/S-20 samples. The excitation wavelength was 365 nm pump light. Fig. 4 presents the 2D pseudocolor images (Figs. 4d, 4e) and representative decay profiles at different delay time (ranging from 50 ps to 6 ns) (Figs. 4f, 4g). The time profiles were analysed at a 640 nm detection wavelength and fitted with a triple exponential equation. The decay kinetics analysis reveals three decay lifetimes: $\tau_1 = 0.19$ ps (32.8%), $\tau_2 = 45.3$ ps (21.5%), and $\tau_3 = 129.6$ ps (45.7%) for pristine g-CN (Figs. 4h, 4i). The fastest τ_1 lifetime corresponding to hot electrons cooling down to the conduction band bottom [60]. Notably, g-CN/S-20 exhibited a similar τ_1 value, indicating a comparable hot electron cooling process to that observed in g-CN. The lifetime τ_2 and τ_3 are related to exciton annihilation and the shallow trapping state, respectively [16]. In g-CN/S-20, there was a notable reduction in the exciton annihilation lifetime compared to pristine g-CN, suggesting a significant effect on charge carrier kinetics. The bandgap exciton annihilation lifetime in g-CN/S-20 was measured to be 14.31 ps (19.8%) (τ_2). The reduced exciton binding energy in g-CN/S-20 results in increased exciton dissociation, leading to a shorter lifetime [59]. On the other hand, the lifetime of the shallow electron trapping state in g-CN/S-20 was significantly prolonged to 565.8 ps (40.0%) compared to g-CN, allowing more active electrons to invovle in photocatalytic reactions. This enhanced charge separation in g-CN/S-20 facilitates a higher participation of electrons in photoreduction reactions, favoring the enhancement in photocatalytic activity [16].

We further conducted density functional theory (DFT) calculations to investigate how S-incorporation impacts the electronic structure of g-

CN. Our calculations considered the substitution of S at the sp²-hybridized N atom (C═N–C), which is consistent with the XPS and NMR results (Fig. 5a). The crystal structure models revealed that S-incorporation in g-CN induced asymmetry due to the different bond length of S═C (0.172 nm) and C═N (0.134 nm) (Fig. 5a). This asymmetry in tri-s-triazine units leads to the n-π * transition. S-incorporated g-CN exhibited slight red-shift in the adsorption edges compared to pristine g-CN. Furthermore, there was a significant increase in absorption around 700 nm, broadening the absorption spectra and enhancing the photoactivity of S-incorporated g-CN (Fig. S22).

Concerning the electronic structures, S-incorporation narrowed of the bandgap from 2.23 eV in pristine g-CN to 2.00 eV in S-incorporated g-CN (Figs. 5c and 5d). Notably, the composition of the conduction band (CB) and valence band (VB) in S-incorporated g-CN remained almost unchanged, except for the presence of a small portion of S 3p orbitals (Fig. 5b). The inset in Fig. 5b shows contribution of S 3p orbitals to the electronic structure of S-incorporated g-CN [35]. Remarkably, S-incorporation induced spin polarization, as illustrated by the variation in spin-up and spin-down states of band structures. This spin polarization arises from the different numbers of valence electrons between N (5) and S (4) atoms, leading to a localized impurity level in the spin-up state between CB and VB [18,61].

Charge distribution analysis showed that S-incorporated g-CN exhibited enhanced charge separation compared to pristine g-CN (Fig. 5e). This was evident by the significantly localized charges around the S atom at the conduction band minimum (CBM) and negligible charges around the S atom at the valence band maximum (VBM) (Fig. 5f). This promoted charge separation is a result of S-incorporation [2].

We further investigated the active site in g-CN/S-20 theoretically. DFT calculations were used to study the model reaction for H_2 generation on g-CN/S-20. The Gibbs free energies of H adsorption (ΔG_{H*}) on representative sites (C, N, and S in Fig. S24a) in g-CN/S-20 were calculated and illustrated in Fig. S24b. Obviously, the N site displayed the smallest ΔG_{H*} value among these indicated sites in g-CN/S-20, suggesting that H^+ reduction on the N site is thermodynamically
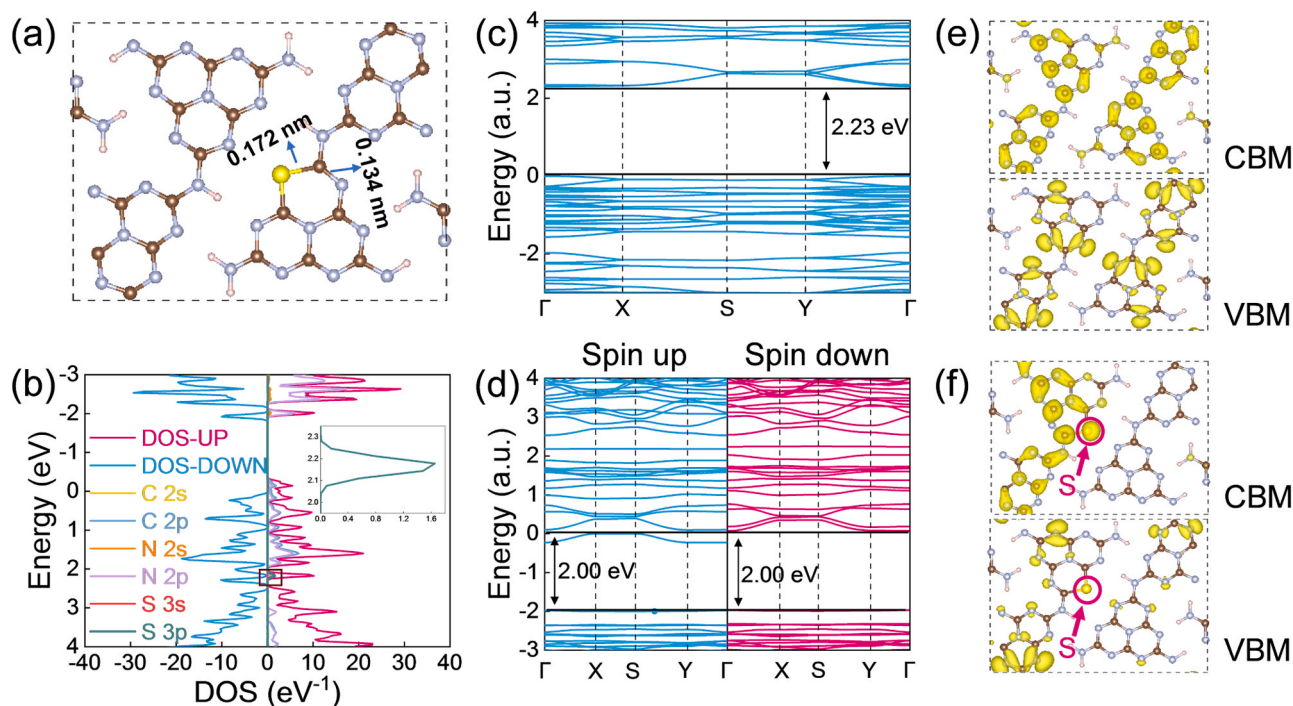

Fig. 5. (a) Structure models of S-incorporated g-CN. Brown, gray, light pink, and yellow balls represent C, N, H, and S atoms, respectively. (b) Density of states in S-incorporated g-CN. Calculated electronic band structure of (c) pristine g-CN and (d) S-incorporated g-CN. Differential charge density of (e) pristine g-CN and (f) S-incorporated g-CN.

favorable. In summary, the DFT calculations demonstrated that S-incorporation increases the availability of electrons, narrows the bandgap, and promotes charge separation, all of which contribute to the remarkably improved photocatalytic H_2 generation in g-CN/S-20.

4. Conclusions

In summary, we successfully engineered n-π * electronic transition in g-CN through thermolysis of urea-NTC aggregates. The modified g-CN demonstrated a red-shifted absorption edge at around 600 nm, expanding its light absorption range. The incorporation of S into g-CN, paticularly g-CN/S-20, reduced the exciton binding energy and significantly extended the lifetime of the shallow trapping states, as revealed by fs-TAS spectroscopy. These enhancements in charge separation efficiency resulted in a remarkable fivefold enhancement in photocatalytic H_2 evolution compared to pristine g-CN. This study highlights the crucial role of the n-π * electronic transition in facilitating charge separation and migration during photocatalysis, providing valuable insights for the development of highly efficient g-C_3N_4-based photocatalysts.

Declaration of Competing Interest

There are no conflicts to declare.

Data Availability

Data will be made available on request.

Acknowledgments

Appendix A. Supporting information

Supplementary data associated with this article can be found in the online version at doi:10.1016/j.apcatb.2023.123453.

References

[1] W. Xing, W. Tu, Z. Han, Y. Hu, Q. Meng, G. Chen, Template-induced high-crystalline g-C_3N_4 nanosheets for enhanced photocatalytic H_2 evolution, ACS Energy Lett. 3 (2018) 514–519, https://doi.org/10.1021/acsenergylett.7b01328.

[2] H. Wang, J. Jiang, L. Yu, J. Peng, Z. Song, Z. Xiong, N. Li, K. Xiang, J. Zou, J. Hsu, T. Zhai, Tailoring advanced N-defective and S-doped g-C_3N_4 for photocatalytic H_2 evolution, Small (2023) 2301116, https://doi.org/10.1002/smll.202301116.

[3] S. Li, Y. Peng, C. Hu, Z. Chen, Self-assembled synthesis of benzene-ring-grafted g-C_3N_4 nanotubes for enhanced photocatalytic H_2 evolution, Appl. Catal. B: Environ. 279 (2020), 119401, https://doi.org/10.1016/j.apcatb.2020.119401.

[4] X. Wu, D. Li, B. Luo, B. Chen, Y. Huang, T. Yu, N. Shen, L. Li, W. Shi, Molecular-level insights on NIR-driven photocatalytic H_2 generation with ultrathin porous S-doped g-C_3N_4 nanosheets, Appl. Catal. B: Environ. 325 (2023), 122292, https://doi.org/10.1016/j.apcatb.2022.122292.

[5] X. Hao, Y. Wang, J. Zhou, Z. Cui, Y. Wang, Z. Zou, Zinc vacancy-promoted photocatalytic activity and photostability of ZnS for efficient visible-light-driven hydrogen evolution, Appl. Catal. B: Environ. 221 (2018) 302–311, https://doi.org/10.1016/j.apcatb.2017.09.006.

[6] P. Chen, X. Dong, M. Huang, K. Li, L. Xiao, J. Sheng, S. Chen, Y. Zhou, F. Dong, Rapid self-decomposition of g-C_3N_4 during gas–solid photocatalytic CO_2 reduction and its effects on performance assessment, ACS Catal. 12 (2022) 4560–4570, https://doi.org/10.1021/acscatal.2c00815.

[7] Y. Lu, W.-J. Yin, K.-L. Peng, K. Wang, Q. Hu, A. Selloni, F.-R. Chen, L.-M. Liu, M.-L. Sui, Self-hydrogenated shell promoting photocatalytic H_2 evolution on anatase TiO2, Nat. Commun. 9 (2018) 2752, https://doi.org/10.1038/s41467-018-05144-1.

[8] Q. Li, F. Zhao, C. Qu, Q. Shang, Z. Xu, L. Yu, J.R. McBride, T. Lian, Two-dimensional morphology enhances light-driven H_2 generation efficiency in CdS

[9] nanoplatelet-Pt Heterostructures, J. Am. Chem. Soc. 140 (2018) 11726–11734, https://doi.org/10.1021/jacs.8b06100.

[9] M. Xiao, L. Zhang, B. Luo, M. Lyu, Z. Wang, H. Huang, S. Wang, A. Du, L. Wang, Molten-salt-mediated synthesis of an atomic nickel co-catalyst on TiO2 for improved photocatalytic H_2 evolution, Angew. Chem. Int. Ed. 59 (2020) 7230–7234, https://doi.org/10.1002/anie.202001148.

[10] L. Su, L. Luo, H. Song, Z. Wu, W. Tu, Z. Wang, J. Ye, Hemispherical shell-thin lamellar WS2 porous structures composited with CdS photocatalysts for enhanced H_2 evolution, Chem. Eng. J. 388 (2020), 124346, https://doi.org/10.1016/j.cej.2020.124346.

[11] J. Wang, S. Wang, A critical review on graphitic carbon nitride (g-C_3N_4)-based materials: Preparation, modification and environmental application, Coord. Chem. Rev. 453 (2022), 214338, https://doi.org/10.1016/j.ccr.2021.214338.

[12] Y. Wang, L. Liu, T. Ma, Y. Zhang, H. Huang, 2D graphitic carbon nitride for energy conversion and storage, Adv. Funct. Mater. 31 (2021), 2102540, https://doi.org/10.1002/adfm.202102540.

[13] W. Wang, X. Bai, Q. Ci, L. Du, X. Ren, D.L. Phillips, Near-field drives long-lived shallow trapping of polymeric C_3N_4 for efficient photocatalytic hydrogen evolution, Adv. Funct. Mater. 31 (2021), 2103978, https://doi.org/10.1002/adfm.202103978.

[14] X. Zhang, L. Lin, D. Qu, J. Yang, Y. Weng, Z. Wang, Z. Sun, Y. Chen, T. He, Boosting visible-light driven solar-fuel production over g-C_3N_4/tetra(4-carboxyphenyl) porphyrin iron (III) chloride hybrid photocatalyst via incorporation with carbon dots, Appl. Catal. B: Environ. 265 (2020), 118595, https://doi.org/10.1016/j.apcatb.2020.118595.

[15] X. Chen, J. Wang, Y. Chai, Z. Zhang, Y. Zhu, Efficient photocatalytic overall water splitting induced by the giant internal electric field of a g-C_3N_4 /rGO/PDIP Z-scheme heterojunction, Adv. Mater. 33 (2021), 2007479, https://doi.org/10.1002/adma.202007479.

[16] Z. Zhang, L. Ren, H. Li, D. Jiang, Y. Fang, H. Du, G. Xu, C. Zhu, H. Li, Z. Lu, Y. Yuan, π-conjugated in-plane heterostructure enables long-lived shallow trapping in graphitic carbon nitride for increased photocatalytic hydrogen generation, Small 19 (2023), 2207173, https://doi.org/10.1002/smll.202207173.

[17] C. Xing, G. Yu, J. Zhou, Q. Liu, T. Chen, H. Liu, X. Li, Solar energy-driven upcycling of plastic waste on direct Z-scheme heterostructure of V-substituted phosphomolybdic acid/g-C_3N_4 nanosheets, Appl. Catal. B: Environ. 315 (2022), 121496, https://doi.org/10.1016/j.apcatb.2022.121496.

[18] C. Feng, L. Tang, Y. Deng, J. Wang, Y. Liu, X. Ouyang, H. Yang, J. Yu, J. Wang, A novel sulfur-assisted annealing method of g-C_3N_4 nanosheet compensates for the loss of light absorption with further promoted charge transfer for photocatalytic production of H_2 and H_2O_2, Appl. Catal. B: Environ. 281 (2021), 119539, https://doi.org/10.1016/j.apcatb.2020.119539.

[19] T. Mahvelati-Shamsabadi, K.C. Bhamu, S. Lee, T.T. Dang, V.H. Khoi, S.H. Hur, W. M. Choi, S.G. Kang, T.J. Shin, J.S. Chung, Coordinatively unsaturated atomically dispersed Pt$_{+2}$-N4 sites on hexagonal nanosheet structure of g-C_3N_4 for high-performance photocatalytic H_2 production, Appl. Catal. B: Environ. 337 (2023), 122959, https://doi.org/10.1016/j.apcatb.2023.122959.

[20] W. Dai, R. Wang, Z. Chen, S. Deng, C. Huang, W. Luo, H. Chen, Highly-efficient photocatalytic hydrogen evolution triggered by spatial confinement effects over co-crystal templated boron-doped carbon nitride hollow nanotubes, J. Mater. Chem. A. 11 (2023) 7584–7595, https://doi.org/10.1039/D3TA00199G.

[21] X. Wu, D. Li, B. Luo, B. Chen, Y. Huang, T. Yu, N. Shen, L. Li, W. Shi, Molecular-level insights on NIR-driven photocatalytic H_2 generation with ultrathin porous S-doped g-C_3N_4 nanosheets, Appl. Catal. B: Environ. 325 (2023), 122292, https://doi.org/10.1016/j.apcatb.2022.122292.

[22] Y. Zhou, L. Zhang, W. Huang, Q. Kong, X. Fan, M. Wang, J. Shi, N-doped graphitic carbon-incorporated g-C_3N_4 for remarkably enhanced photocatalytic H_2 evolution under visible light, Carbon 99 (2016) 111–117, https://doi.org/10.1016/j.carbon.2015.12.008.

[23] X. Tian, Y. Sun, J. He, X. Wang, J. Zhao, S. Qiao, F. Li, Surface P atom grafting of g-C_3N_4 for improved local spatial charge separation and enhanced photocatalytic H_2 production, J. Mater. Chem. A 7 (2019) 7628–7635, https://doi.org/10.1039/C9TA00129H.

[24] G. Zhao, B. Li, X. Yang, X. Zhang, Z. Li, D. Jiang, H. Du, C. Zhu, H. Li, C. Xue, Y. Yuan, two birds with one stone: Engineering polymeric carbon nitride with n-π* electronic transition for extending light absorption and reducing charge recombination, Adv. Powder Mater. 2 (2023), 100077, https://doi.org/10.1016/j.apmate.2022.100077.

[25] G. Zhang, G. Li, Z.-A. Lan, L. Lin, A. Savateev, T. Heil, S. Zafeiratos, X. Wang, M. Antonietti, Optimizing optical absorption, exciton dissociation, and charge transfer of a polymeric carbon nitride with ultrahigh solar hydrogen production activity, Angew. Chem. Int. Ed. 56 (2017) 13445–13449, https://doi.org/10.1002/anie.201706870.

[26] T. Zhou, J. Shi, G. Li, B. Liu, B. Hu, G. Che, C. Liu, L. Wang, L. Yan, Advancing n-π* electron transition of carbon nitride via distorted structure and nitrogen heterocycle for efficient photodegradation: Performance, mechanism and toxicity insight, J. Colloid Interface Sci. 632 (2023) 285–298, https://doi.org/10.1016/j.jcis.2022.11.073.

[27] S. Hu, D. Jiang, L. Gu, G. Xu, Z. Li, Y. Yuan, Awakening n → π* electronic transition by breaking hydrogen bonds in graphitic carbon nitride for increased photocatalytic hydrogen generation, Chem. Eng. J. 399 (2020), 125847, https://doi.org/10.1016/j.cej.2020.125847.

[28] X. Lin, H. Du, D. Jiang, P. Zhang, Z. Yu, H. Bi, Y. Yuan, Microwave awakening the n-π* electronic transition in highly crystalline polymeric carbon nitride nanosheets for photocatalytic hydrogen generation, J. Energy Chem. 65 (2022) 541–547, https://doi.org/10.1016/j.jechem.2021.07.002.

L

[29] J. Xu, M. Fujitsuka, S. Kim, Z. Wang, T. Majima, Unprecedented effect of CO_2 calcination atmosphere on photocatalytic H_2 production activity from water using g-C_3N_4 synthesized from triazole polymerization, Appl. Catal. B: Environ. 241 (2019) 141–148, https://doi.org/10.1016/j.apcatb.2018.09.023.

[30] J. Zhang, W. Zhang, L. Yue, X. Hu, H. Lin, L. Zhao, Y. He, Thiophene insertion and lanthanum molybdate modification of g-C_3N_4 for enhanced visible-light-driven photoactivity in tetracycline degradation, Appl. Surf. Sci. 592 (2022), 153337, https://doi.org/10.1016/j.apsusc.2022.153337.

[31] Y. Li, X. Pang, Q. Zhao, B. Zhang, X. Guo, Y. Zhang, Y. Xie, C. Qin, L. Jing, Controlled synthesis of nitro-terminated oligothiophene/crystallinity-improved g-C_3N_4 heterojunctions for enhanced visible-light catalytic H_2 production, ACS Appl. Mater. Interfaces 15 (2023) 5365–5377, https://doi.org/10.1021/acsami.2c21849.

[32] Y. Li, J. Chen, P. Cai, Z. Wen, An electrochemically neutralized energy-assisted low-cost acid-alkaline electrolyzer for energy-saving electrolysis hydrogen generation, J. Mater. Chem. A. 6 (2018) 4948–4954, https://doi.org/10.1039/C7TA10374C.

[33] M. Kamal Hussien, A. Sabbah, M. Qorbani, M. Hammad Elsayed, P. Raghunath, T.-Y. Lin, S. Quadir, H.-Y. Wang, H.-L. Wu, D.-L.M. Tzou, M.-C. Lin, P.-W. Chung, H.-H. Chou, L.-C. Chen, K.-H. Chen, Metal-free four-in-one modification of g-C_3N_4 for superior photocatalytic CO_2 reduction and H_2 evolution, Chem. Eng. J. 430 (2022), 132853, https://doi.org/10.1016/j.cej.2021.132853.

[34] J. Cheng, Z. Hu, Q. Li, X. Li, S. Fang, X. Wu, M. Li, Y. Ding, B. Liu, C. Yang, L. Wen, Y. Liu, K. Lv, Fabrication of high photoreactive carbon nitride nanosheets by polymerization of amidinourea for hydrogen production, Appl. Catal. B: Environ. 245 (2019) 197–206, https://doi.org/10.1016/j.apcatb.2018.12.044.

[35] C. Yang, S. Zhang, Y. Huang, K. Lv, S. Fang, X. Wu, Q. Li, J. Fan, sharply increasing the visible photoreactivity of g-C_3N_4 by breaking the intralayered hydrogen bonds, Appl. Surf. Sci. 505 (2020), 144654, https://doi.org/10.1016/j.apsusc.2019.144654.

[36] Y.-R. Lin, G.V.C. Dizon, K. Yamada, C.-Y. Liu, A. Venault, H.-Y. Lin, M. Yoshida, C. Hu, Sulfur-doped g-C_3N_4 nanosheets for photocatalysis: Z-scheme water splitting and decreased biofouling, J. Colloid Interface Sci. 567 (2020) 202–212, https://doi.org/10.1016/j.jcis.2020.02.017.

[37] Y. Li, J. Chen, P. Cai, Z. Wen, An electrochemically neutralized energy-assisted low-cost acid-alkaline electrolyzer for energy-saving electrolysis hydrogen generation, J. Mater. Chem. A. 6 (2018) 4948–4954, https://doi.org/10.1039/C7TA10374C.

[38] J. Xiao, J. Rabeah, J. Yang, Y. Xie, H. Cao, A. Brückner, Fast electron transfer and $^{\bullet}$OH formation: key features for high activity in visible-light-driven ozonation with C_3N_4 catalysts, ACS Catal. 7 (2017) 6198–6206, https://doi.org/10.1021/acscatal.7b02180.

[39] Y. Zhang, S. Zong, C. Cheng, J. Shi, P. Guo, X. Guan, B. Luo, S. Shen, L. Guo, Rapid high-temperature treatment on graphitic carbon nitride for excellent photocatalytic H_2-evolution performance, Appl. Catal. B: Environ. 233 (2018) 80–87, https://doi.org/10.1016/j.apcatb.2018.03.104.

[40] C. Zhang, Z. Ouyang, Y. Yang, X. Long, L. Qin, W. Wang, Y. Zhou, D. Qin, F. Qin, C. Lai, Molecular engineering of donor-acceptor structured g-C_3N_4 for superior photocatalytic oxytetracycline degradation, Chem. Eng. J. 448 (2022), 137370, https://doi.org/10.1016/j.cej.2022.137370.

[41] S. Bellamkonda, R. Shanmugam, R.R. Gangavarapu, Extending the π-electron conjugation in 2D planar graphitic carbon nitride: efficient charge separation for overall water splitting, J. Mater. Chem. A. 7 (2019) 3757–3771, https://doi.org/10.1039/C8TA10580D.

[42] Y. Wang, M.K. Bayazit, S.J.A. Moniz, Q. Ruan, C.C. Lau, N. Martsinovich, J. Tang, Linker-controlled polymeric photocatalyst for highly efficient hydrogen evolution from water, Energy Environ. Sci. 10 (2017) 1643–1651, https://doi.org/10.1039/C7EE01109A.

[43] Y.P. Zhu, Y. Lei, F. Ming, E. Abou-Hamad, A.-H. Emwas, M.N. Hedhili, H.N. Alshareef, Heterostructured MXene and g-C_3N_4 for high-rate lithium intercalation, Nano Energy 65 (2019), 104030, https://doi.org/10.1016/j.nanoen.2019.104030.

[44] X. Li, I.V. Sergeyev, F. Aussenac, A.F. Masters, T. Maschmeyer, J.M. Hook, Dynamic nuclear polarization NMR spectroscopy of polymeric carbon nitride photocatalysts: insights into structural defects and reactivity, Angew. Chem. Int. Ed. 57 (2018) 6848–6852, https://doi.org/10.1002/anie.201802278.

[45] Y. Hu, Y. Shim, J. Oh, S. Park, S. Park, Y. Ishii, Synthesis of ^{13}C-, ^{15}N-labeled graphitic carbon nitrides and nmr-based evidence of hydrogen-bonding assisted

[46] two-dimensional assembly, Chem. Mater. 29 (2017) 5080–5089, https://doi.org/10.1021/acs.chemmater.7b00069.

[47] P. Zeng, W.-D. Zhang, Photocatalytic hydrogen evolution over a nickel complex anchoring to thiophene embedded g-C_3N_4, J. Colloid Interface Sci. 596 (2021) 75–88, https://doi.org/10.1016/j.jcis.2021.03.080.

[48] J. Jiang, Z. Xiong, H. Wang, G. Liao, S. Bai, J. Zou, P. Wu, P. Zhang, X. Li, Sulfur-doped g-C_3N_4/g-C_3N_4 isotype step-scheme heterojunction for photocatalytic H_2 evolution, J. Mater. Sci. Technol. 118 (2022) 15–24, https://doi.org/10.1016/j.jmst.2021.12.018.

[49] L. Xu, B. Tian, T. Wang, Y. Yu, W. Wu, J. Cui, Z. Cao, J. Wu, W. Zhang, Q. Zhang, J. Liu, Z. Li, Y. Tian, Direct Z-scheme polymeric heterojunction boosts photocatalytic hydrogen production via a rebuilt extended π-delocalized network, Energy Environ. Sci. 15 (2022) 5059–5068, https://doi.org/10.1039/D2EE02380F.

[50] S. Hou, G. Gao, S. Wang, X. Yu, J. Liao, D. Su, Precise defect engineering on graphitic carbon nitrides for boosted solar H_2 production, Small (2023), 2302500, https://doi.org/10.1002/smll.202302500.

[51] E. Liu, X. Lin, Y. Hong, L. Yang, B. Luo, W. Shi, J. Shi, Rational copolymerization strategy engineered C self-doped g-C_3N_4 for efficient and robust solar photocatalytic H_2 evolution, Renew. Energy 178 (2021) 757–765, https://doi.org/10.1016/j.renene.2021.06.066.

[52] X. Li, J. Yu, J. Low, Y. Fang, J. Xiao, X. Chen, Engineering heterogeneous semiconductors for solar water splitting, J. Mater. Chem. A. 3 (2015) 2485–2534, https://doi.org/10.1039/C4TA04461D.

[53] Y. Huang, J. Liu, C. Zhao, X. Jia, M. Ma, Y. Qian, C. Yang, K. Liu, F. Tan, Z. Wang, X. Li, S. Qu, Z. Wang, Facile synthesis of defect-modified thin-layered and porous g-C_3N_4 with synergetic improvement for photocatalytic H_2 production, ACS Appl. Mater. Interfaces 12 (2020) 52603–52614, https://doi.org/10.1021/acsami.0c14262.

[54] F. Ge, S. Huang, J. Yan, L. Jing, F. Chen, M. Xie, Y. Xu, H. Xu, H. Li, Sulfur promoted n-π* electron transitions in thiophene-doped g-C_3N_4 for enhanced photocatalytic activity, Chin. J. Catal. 42 (2021) 450–459, https://doi.org/10.1016/S1872-2067(20)63674-9.

[55] X. Zhao, J. Li, X. Kong, C. Li, B. Lin, F. Dong, G. Yang, G. Shao, C. Xue, Carbon dots mediated in situ confined growth of Bi clusters on g-C_3N_4 nanomeshes for boosting plasma-assisted photoreduction of CO_2, Small 18 (2022), 2204154, https://doi.org/10.1002/smll.202204154.

[56] Q. Cheng, Y.-J. Yuan, R. Tang, Q.-Y. Liu, L. Bao, P. Wang, J. Zhong, Z. Zhao, Z.-T. Yu, Z. Zou, Rapid hydroxyl radical generation on (001)-facet-exposed ultrathin anatase TiO_2 nanosheets for enhanced photocatalytic lignocellulose-to-H_2 conversion, ACS Catal. 12 (2022) 2118–2125, https://doi.org/10.1021/acscatal.1c05713.

[56] Y. Wang, X. Zhang, X. Ding, Y. Li, B. Wu, P. Zhang, X. Zeng, Q. Zhang, Y. Du, Y. Gong, K. Zheng, X. Tian, Stitching graphene sheets with graphitic carbon nitride: constructing a highly thermally conductive rGO/g-C_3N_4 film with excellent heating capability, ACS Appl. Mater. Interfaces 13 (2021) 6699–6709, https://doi.org/10.1021/acsami.0c22057.

[57] J. Xu, C. Yang, S. Bi, W. Wang, Y. He, D. Wu, Q. Liang, X. Wang, F. Zhang, Vinylene-linked covalent organic frameworks (COFs) with symmetry-tuned polarity and photocatalytic activity, Angew. Chem. Int. Ed. 59 (2020) 23845–23853, https://doi.org/10.1002/anie.202011852.

[58] J. Zhang, Y. Yang, H. Deng, U. Farooq, X. Yang, J. Khan, J. Tang, H. Song, High quantum yield blue emission from lead-free inorganic antimony halide perovskite colloidal quantum dots, ACS Nano 11 (2017) 9294–9302, https://doi.org/10.1021/acsnano.7b04683.

[59] C. Li, J. Liu, H. Li, K. Wu, J. Wang, Q. Yang, Covalent organic frameworks with high quantum efficiency in sacrificial photocatalytic hydrogen evolution, Nat. Commun. 13 (2022) 2357, https://doi.org/10.1038/s41467-022-30035-x.

[60] L. Zhu, Z. Liang, H. Li, Q. Xu, D. Jiang, H. Du, C. Zhu, H. Li, Z. Lu, Y. Yuan, A π-conjugated van der waals heterostructure between single-atom Ni-anchored salphen-based covalent organic framework and polymeric carbon nitride for high-efficiency interfacial charge separation, Small (2023), 2301017, https://doi.org/10.1002/smll.202301017.

[61] Y. Tong, C. Wei, Y. Li, Y. Zhang, W. Lin, Unraveling the mechanisms of S-doped carbon nitride for photocatalytic oxygen reduction to H_2O_2, Phys. Chem. Chem. Phys. 22 (2020) 21099–21107, https://doi.org/10.1039/D0CP03533E.